TROPOSPHERIC EMISSION SPECTROMETER (TES)

LEVEL 2 ALGORITHM THEORETICAL BASIS DOCUMENT APPENDIX

Reinhard Beer	Jet Propulsion Laboratory
Kevin W. Bowman	Jet Propulsion Laboratory
Patrick D. Brown	Atmospheric and Environmental Research Inc.
Shepard A. Clough	Atmospheric and Environmental Research Inc.
Aaron Goldman	University of Denver
Daniel J. Jacob	Harvard University
Jennifer A. Logan	Harvard University
Mingzhao Luo	Jet Propulsion Laboratory
Frank J. Murcray	University of Denver
David M. Rider	Jet Propulsion Laboratory
Curtis P. Rinsland	NASA Langley Research Center
Clive D. Rodgers	University of Oxford
Stanley P. Sander	Jet Propulsion Laboratory
Eugene Ustinov	Jet Propulsion Laboratory
Helen M. Worden	Jet Propulsion Laboratory
Marguerite Syvertson, editor	Jet Propulsion Laboratory

Approved by:
Reinhard Beer
TES Principal Investigator

Version 1.1
October 1, 1999

Jet Propulsion Laboratory
California Institute of Technology
Pasadena, California

I. TABLE OF CONTENTS

II. LIST OF FIGURES

III. LIST OF TABLES

THIS PAGE INTENTIONALLY LEFT BLANK.

APPENDICES

A3.3.1: Radiative Transfer

The Radius of Curvature of the Earth's Surface for a Given TES Limb Tangent Latitude and Viewing Direction

The ray-tracing step in Level 2 process uses Snell's Law for a spherically symmetric atmosphere to determine the bending along the ray. The radius of the "sphere" is considered to be the sum of the altitude and the *radius of curvature of the Earth surface* (not the Earth-centered radius) at the given location in the given direction. This Appendix presents the equations for the radius of the Earth surface curvature at a given latitude (TES limb tangent latitude) for TES viewing direction.

A very commonly used Earth geometric model is an ellipsoidal shape as illustrated below.

Figure A - 1: Earth Geometric Model
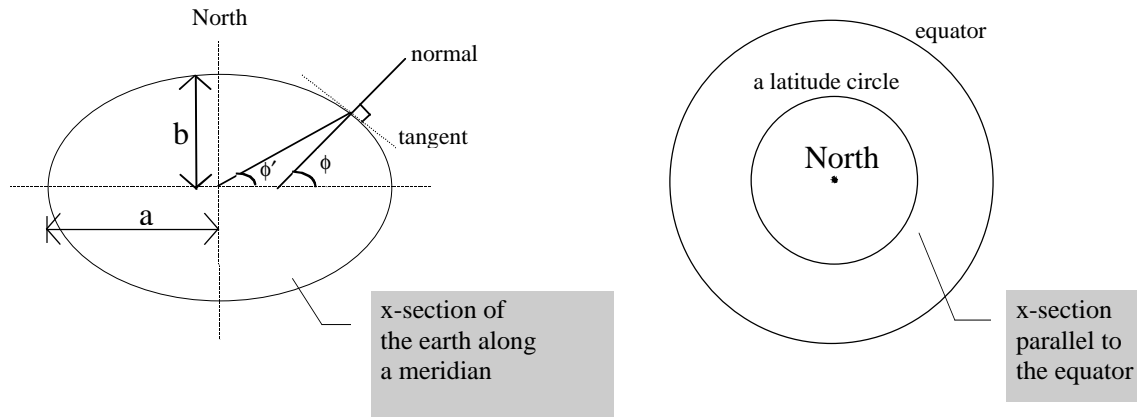
Definitions of some parameters:

a   —   equatorial radius (the semi-major axis of the meridian ellipse).
b   —   polar radius (the semi-minor axis of the meridian ellipse).
f   —   flattening factor.
e   —   Earth ellipsoid eccentricity.
ϕ —   geodetic latitude as illustrated above.
ϕ' —   geocentric latitude as illustrated above.

Their relationships:

$$\tan(\phi) = \frac{\tan(\phi')}{(1-f)^2}; \tag{A1.1}$$

$$f = \frac{a - b}{a}; \text{ and} \qquad\qquad (A1.2)$$

$$e = \sqrt{2f - f^2}. \qquad\qquad (A1.3)$$

There are two principle curvatures on the model Earth surface at a given location, the meridian curvature (North-South curvature) and the East-West curvature. The tangents of these two curvature are perpendicular. The East-West curvature plane is defined by the tangent along a latitude circle and the local normal. The equations for the radius of these two principle curvature planes are:

Radius of curvature in the North-South plane:

$$R_{NS} = \frac{a(1 - e^2)}{(1 - e^2 \sin^2\phi)^{3/2}}. \qquad\qquad (A1.4)$$

Radius of curvature in the East-West plane:

$$R_{EW} = \frac{a}{(1 - e^2 \sin^2\phi)^{1/2}}. \qquad\qquad (A1.5)$$

TES always looks straight backward along the orbit. The orbit has 98.21° inclination angle which is the angle between the equatorial plane and the orbital plane. The parameter to define the TES viewing direction at its limb tangent point or any point along its line of sight is the *azimuth angle* (A_Z). The azimuth angle is the angle between the local meridian plane (the N-S plane) and the plane defined by the local normal and the tangent along the TES viewing direction. Under the spherical approximation, A_Z can be calculated as

$$\sin(A_z) = \frac{\cos(\text{inclination angle})}{\cos(\text{geocentric latitude})}. \qquad\qquad (A1.6)$$

The EOS Toolkit provides a program to calculate a more rigorous azimuth without the spherical approximation (PGS_CSC_ZenithAzimuth). The viewing vector however, in the ECR (Earth Centered Rotating) coordinate system, needs to be defined.

The radius of the curvature in azimuth A_Z (R_C) can be calculated as

Radius of curvature in azimuth A_Z:

$$\frac{1}{R_C} = \frac{\cos^2(A_z)}{R_{NS}} + \frac{\sin^2(A_z)}{R_{EW}}. \qquad\qquad (A1.7)$$

A3.3.1.1: Ray Tracing and Path Integrals

For ray tracing and path integrals, we require the following elements from the retrieval vector, at a set of levels $j=0..n$ in $\ln(P)$, and in the limb case when the atmosphere is not horizontally homogeneous, also at a set of locations along the line of sight:

T_j level temperatures
q_{jm} level mixing ratios for molecule m
P_s surface pressure
T_s surface temperature

and the following forward model parameters:

z_s altitude of the surface relative to the geoid
R_c radius of the geoid at the measurement location
R_{cs} altitude of the spacecraft from the center of curvature of the geoid
θ_s angle of ray at the satellite

The level quantities in the retrieval vector are interpolated at a finer spacing to give the full grid level values $q_k{}^m$ and T_k.

A3.3.1.1.1 Hydrostatic Equation

The total air density ρ_k is computed from the gas equation at each full grid level. This must allow for the water content of the air, but the other minor constituents may be ignored [except possibly CO_2] (see Appendix 3.3.1.1.7). The hydrostatic equation may be written

$$dz = -[P/\rho(P)g(z)] \, d \ln(P) \qquad\qquad (A2.1)$$

As the quantity $[P/\rho(z)g(z)]$ is close to RT/Mg, from the ideal gas equation, we take it to be linear in $\ln(P)$ over each layer. Hence the layer thickness is

$$z_k - z_{k-1} = (P_{k-1}/\rho_{k-1}g_{k-1} + P_k/\rho_k g_k)[\ln(P_{k-1}) - \ln(P_k)]/2 \qquad\qquad (A2.2)$$

from the trapezoidal rule. The acceleration due to gravity is given as a function of height and latitude, and it consists of gravitational and rotational parts,

$$g(\phi, z) = g_{grav}(\phi,0)[(R_e)/(R_e + z)]^2 - \Omega^2 N[((N+z)/R_e)\cos \phi]^2 \qquad\qquad (A2.3)$$

where Ω is the Earth's rotational angular frequency; $N = a^2 \sqrt{(a^2 - (a^2 - b^2)\sin^2 \phi)}$; and a and b is the semi-major and minor axis of earth respectively. The gravitational term at the earth surface is given by [International Gravity Formula, 1980]

$$g(\phi,0) = 978.0327(1.0 + 0.0052790414\sin^2 \phi + 0.0000232718\sin^4 \phi + 0.0000001262\sin^6 \phi,$$

$$\text{and } g_{grav}(\phi,0) = g(\phi,0) - g_{rot}(\phi,0). \tag{A2.4}$$

Note that equation (A2.2) requires $g_k = g(z_k)$ before z_k has been computed. The effect is small and can be accommodated by several different ways, of which the simplest might be to approximate g_k by its value at an altitude given by $2z_{k-1}-z_{k-2}$.

A3.3.1.1.2 Ray tracing in the nadir case.

The zenith angle of the ray at each level is given by Snell's law in spherical symmetry:

$$\sin\theta_k = [R_{cs}\sin\theta_s]/[(R_c + z_k)n_k] \tag{A.2.5}$$

where the refractive index n_k is given in section A3.3.1.1.8. However as $n_k \sim 1.0002$ at the surface, it may be ignored, incurring an error of only 0.02% in $\sin\theta_k$, and hence a similarly small amount in path length through $\sec\theta_k$.

A3.3.1.1.3 Path integrals in the nadir case

We need to evaluate the number of molecules per unit area in each layer, together with appropriately weighted mean pressures and temperatures of the layer. The mass per unit area of an element dP is dP/g, so the number of molecules of molecule m is

$$dn_m = Nq_m dP/g[M_d + q^w M_w] \tag{A.2.6}$$

where N is Avogadro's number, q_m is the volume mixing ratio of molecule m, defined as the ratio to the number of molecules of *dry* air, M_d and M_w are the molar masses of dry air and water, and q^w is the mixing ratio of water vapor. Hence the number of molecules of m in a layer along the line of sight is

$$u_{lm} = -\int l_{l-1} q_m(P)f(P)\,dP \tag{A.2.7}$$

where

$$f(P) = \sec\theta\, N/g[M_d + q^w M_w] \tag{A.2.8}$$

is very nearly constant over a layer. Interpolating $\ln(f)$ as well as $\ln(q_m)$ linearly in $\ln(P)$, we obtain integrals that can be evaluated analytically. Putting

$$q_m f = q_{ml-1}f_{l-1}(P/P_{l-1})^{\alpha l} \tag{A.2.9}$$

within the layer, where $\alpha_l = \ln(q_{ml}f_l/q_{ml-1}f_{l-1})/(\zeta_l - \zeta_{l-1})$, we obtain
$$u_{lm} = [q_{ml-1}f_{l-1}P_{l-1} - q_{ml}f_l P_l]/(1+\alpha_l)$$
$$= q_{ml-1}f_{l-1}P_{l-1}(\zeta_l - \zeta_{l-1})E[(1+\alpha_l)(\zeta_l - \zeta_{l-1})] \tag{A.2.10}$$

where $E(x) = [1-\exp(-x)]/x$, which will need special evaluation near $x=0$. The first form is simpler, but the second form is needed when $(1+\alpha_l)\sim 0$. We also require the weighted mean pressure and temperature obtained from

$$u_{lm}\overline{P}_l = -\int l_{l-1} q_m f\, P\, dP \tag{A.2.11}$$

4

$$u_{lm}\overline{T}_l = -\int l_{l-1} \, q_m f \, T \, dP \tag{A.2.12}$$

in order to evaluate the optical depth

$$\tau_v = k_v(\overline{P}, \overline{T}) \, u \tag{A.2.13}$$

where k_v is the absorption coefficient (cross section) to be interpolated from a tabulation against pressure and temperature. We easily obtain

$$\begin{aligned} u_{lm}\overline{P}_l &= [q_{ml-1}f_{l-1}P^2_{l-1} - q_{ml}f_l P^2_l]/(2+\alpha_l) \\ &= q_{ml-1}f_{l-1}P^2_{l-1}(\zeta_l - \zeta_{l-1})E[(2+\alpha_l)(\zeta_l - \zeta_{l-1})] \end{aligned} \tag{A.2.14}$$

The temperature integral can also be performed algebraically, but leads to slightly more complicated expressions.

For computational efficiency we wish to avoid a two dimensional interpolation in the absorption coefficient tables. The mean pressure is therefore approximated by its value at $\alpha_l = 0$, and the tabulation made at the corresponding set of layer mean pressures, $\overline{P}_l = (P_l + P_{l-1})/2$. This approximation is in error by 1.2% in pressure at $\alpha = <1$ for a layer thickness of 1 UARS layer, and is quadratic in layer thickness.

A3.3.1.1.4 Ray Tracing in the Limb Case

To avoid a pressure interpolation in the absorption coefficient table in the forward model, we need to predetermine the layer mean pressures in order to tabulate at the required pressures. Therefore we ray trace forward from a set of tangent points on the full grid (with given pressures) and evaluate the forward model for these rays, rather than tracing from the satellite in a set of directions related to the detector array. The ray trace will provide an angle of incidence at the satellite, so that a quadrature over the field of view of each detector can be carried out.

The use of a pressure grid involves an extra complication, because ray tracing is essentially a geometric procedure, best carried out in height coordinates, while the state vector is defined in pressure coordinates. In the case when horizontal homogeneity is assumed, the approach is relatively straightforward, following the principles of the method used in Kneizys *et al*. (1983). The quantities required from the ray trace are the angle of the ray at the satellite, and the pressure as a function of distance along the ray, so that path integrals such as $\int q\rho \, ds$, $\int q\rho P \, ds$, and $\int \rho T \, ds$ can be evaluated for each layer.

Figure A - 2: Propagation of a refracted ray through the limb
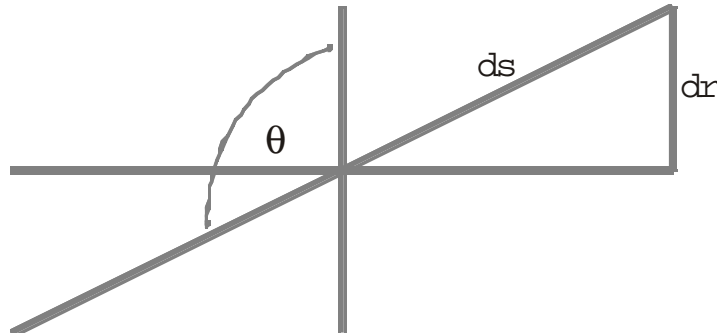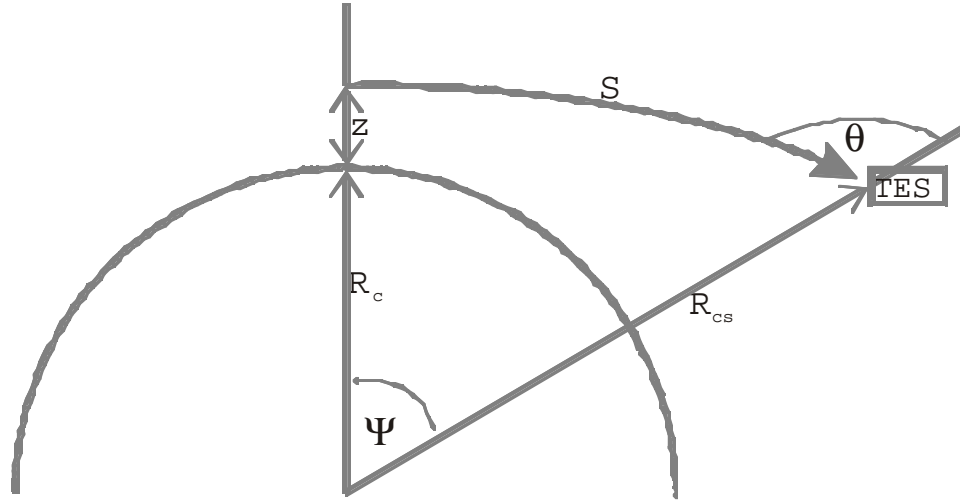
First we use the hydrostatic equation to obtain the heights z_k of the pressure levels for the full grid. These will not be equally spaced in height. We then trace a ray from each z_k as tangent height to the altitude of the satellite, relative to the center of curvature of the geoid. See Figure A-2 to define the terminology. For the refracted ray in the horizontally homogeneous case, the zenith angle of the ray at any altitude can be obtained from Snell's law:

$$n(r)r \sin\theta(r)= r_m \tag{A.2.15}$$

where $r = z+R_c$ and $r_g = n(r_t)r_t =R_{cs} \sin\theta_s$, is a constant for the ray, the geometric tangent radius or the *impact parameter*. Using

$$dr = \cos\theta \, ds \tag{A.2.16}$$

we obtain

$$ds = (1 - r_g^2/n^2r^2)^{-1/2} \, dr \tag{A.2.17}$$

which cannot easily be integrated numerically to obtain $s(r)$ because of the singularity at the tangent point. However by changing the variable of integration from r to $x = r\cos\theta$ we can obtain

$$ds = dx/[1-\gamma(r)\sin^2\theta(r)] \qquad (A.2.18)$$

where $\gamma = -(r/n)\partial n/\partial r$, a positive quantity, is an explicit function of r, as is $\sin\theta$. The coordinate x has the property that in the absence of refraction, $x = s$. To integrated over each full grid layer, we choose a set of quadrature points xl within the layer, and use e.g. the trapezium rule:

$$\Delta s = \Sigma_i (x_i - x_{i-1})(1/(1-\gamma_i\sin^2\theta_i) + 1/(1-\gamma_{i-1}\sin^2\theta_{i-1}))/2 \qquad (A.2.19)$$

or some higher order integration rule. Note that it is not straightforward to find the altitudes of a set of points equally spaced in x because $x^2 = r^2 - r_g^2/n^2(r)$ cannot be explicitly inverted to give $r(x)$, even though x can be evaluated at any given value of r. Either $r^2(x) = x^2 + r_g2/n^2(r)$ must be evaluated iteratively, or points chosen in r^2 to make them approximately evenly spaced in x.

The refractive index of air is given in section A3.3.1.1.8 as an experimentally fitted function of pressure, temperature and water vapor. However it is close to being of the form $n = 1 + \alpha\rho(r)$, where α is a constant, so that within each narrow layer, such as the full grid layer, it may be reasonably fitted to the form

$$n = 1 + \alpha\rho_0 \exp(-r/H_n) \qquad (A.2.20)$$

so that we can write

$$\partial n/\partial r = -(n - 1)/H_n \qquad (A.2.21)$$

where H_n is the scale height of refractivity, n-1, within the layer.

A3.3.1.1.5 Path Integrals for the Limb Case

The absorber amount of molecule m in a sublayer, $\Delta u_m = \int q_m\rho \, ds$ can be evaluated in the same way as Δs by integrating with respect to x using the trapezium (or other) rule:

$$\Delta u_m = \Sigma_l (x_l - x_{l-1})(q_{lm}\rho_l/(1-\gamma_l\sin^2\theta_l) + q_{ml-1}\rho_{l-1}/(1-\gamma_{l-1}\sin^2\theta_{l-1}))/2 \qquad (A.2.22)$$

The effective pressure for a full grid layer is defined by

$$\overline{P} = \int\rho P \, ds/ \int\rho \, ds \qquad (A.2.23)$$

where the two integrals are evaluated as sums over sublayers within the full grid layer, the elements of the sums being

$$\int\rho P \, ds = \Delta(uP) = \Sigma_i (x_i - x_{i-1})(P_i\rho_i/(1-\gamma_i\sin^2\theta_i) + P_{i-1}\rho_{i-1}/(1-\gamma_{i-1}\sin^2\theta_{i-1}))/2 \quad (A.2.24)$$

and

$$\int\rho \, ds = \Delta u = \Sigma_i (x_i - x_{i-1})(\rho_i/(1-\gamma_i\sin^2\theta_i) + \rho_{i-1}/(1-\gamma_{i-1}\sin^2\theta_{i-1}))/2 \qquad (A.2.25)$$

The integral over the lowest sublayers (close to the tangent point) should be evaluated using a quadratic rule.

The effective temperature for a full grid layer is defined by

$$\overline{T} = \int \rho T \, ds / \int \rho \, ds \tag{A.2.26}$$

in a similar way to the effective pressure. The elements of the sum for the numerator are

$$\Delta(uT) = \Sigma_i (x_i - x_{i-1})(T_i \rho_i / (1 - \gamma_i \sin^2 \theta_i) + T_{i-1} \rho_{i-1} / (1 - \gamma_{i-1} \sin^2 \theta_{i-1})) / 2 \tag{A.2.27}$$

Again, the integral over the lowest sublayers should be evaluated using a quadratic rule.

A3.3.1.1.6 Ray tracing in the Inhomogeneous Limb Case.

It is marginal whether the change in the refracted path due to horizontal inhomogeneities is significant. In the worst case, the slope of a pressure surface of 0.001, corresponding to a geostrophic wind of 100 m s^{-1}, gives an error in tangent height at mid troposphere of order 40 m, or about 0.5% in pressure or density. Nevertheless we give the following analysis to describe a possible approach, should it be needed on further investigation.

In the general case the refraction equations do not have an explicit solution expressible as integrals, unlike the horizontally homogeneous case. A set of coupled ordinary differential equations can be derived, relating $r(s)$, $\theta(s)$ and $\psi(s)$:

$$d(\theta + \psi)/ds = -\sin\theta /n \, (\partial n/\partial r)_\psi + (\cos\theta /rn)(\partial n/\partial \psi)_r \tag{A.2.28}$$
$$dr/ds = \cos\theta \tag{A.2.29}$$
$$d\psi/ds = \sin\theta /r \tag{A.2.30}$$

where ψ is the angle at the center of curvature relative to the instrument. The first equation states that the curvature of the ray is equal to the fractional gradient of the refractive index normal to the ray. The others are simple geometry. We can use **(A.2.28)** and **(A.2.30)** to obtain:

$$d\theta/ds = -\sin\theta[1/r + 1/n \, (\partial n/\partial r)_\psi] + (\cos\theta /rn)(\partial n/\partial \psi)_r \tag{A.2.31}$$

Equations **(A.2.29), (A.2.30)** and (**A.2.31)** can be integrated by any standard differential equation solver such as Runge-Kutta to give $r(s)$, $\theta(s)$ and $\psi(s)$.

The boundary conditions cause difficulties, however. A single ray must pass through the instrument at a known location, and have a tangent point at a given pressure level:

(i)   at $s = 0$, $\psi(0) = 0$ and $r(0) = R_{cs}$
(ii)   at $r = r(\zeta_i)$, $\cot\theta = - (1/r)(\partial r/\partial \psi)_\zeta$, i.e the slope of pressure surface ζ_i

where $\zeta = -\ln(P/P_0)$. Here I have put the origins of ψ and s at the instrument for convenience. We do not know before the ray trace where ψ of the tangent point is relative to the satellite. (This does not matter in the case of the horizontally homogeneous atmosphere.) Therefore we must solve the problem iteratively by either:

(a) finding the value of ψ at the tangent point for which the ray passes through the instrument, or
(b) finding the scan angle θ_s at the satellite which gives a tangent point at the right pressure level

To locate the tangent point relative to the satellite, it is most convenient to locate the origin of *s* at the tangent point and the origin of ψ at the instrument. The initial conditions are, at the tangent point

$$\text{(i) } s = 0 \quad \text{(ii) } r = r_t \quad \text{(iii) } \psi = \psi_t \quad \text{(iv) } \cot\theta = -(1/r)(\partial r/\partial\psi)_\zeta.$$

Integrate forward from the tangent point until the ray reaches satellite altitude R_{cs}. The ray will miss the instrument by an amount $\psi(R_{cs})$. This quantity is then subtracted from ψ_t for the next iteration. If there were no line of sight gradients, we would need to go no further, but one more iteration will probably be necessary for convergence.

The temperature, water and (hence) the refractive index are specified vertically on the full grid, and horizontally at some set of values of ψ. Use the hydrostatic equation to find *r* on this same grid. Then the table can be used to find the partial derivatives $(\partial n/\partial r)_\psi$, $(\partial n/\partial\psi)_r$ and $(\partial r/\partial\psi)_\zeta$ where they are required.

There is the extra complication that we want to find quadrature points along the rays lying on the full grid. We are at liberty to choose the quadrature points for the integration so we will change them as we iterate so that a subset ends up lying on the pressure grid. The suggested process is as follows, for each full grid level within the range seen by the instrument:

Repeat:
   - Select a set of quadrature points in s:
   - First time round, use s = ih, i=0,1.. for some constant spacing h.
   - Subsequent times we will have a reasonable guess at the ray path, so use the tangent point, plus points where the ray intersects the full grid (inverse interpolate in $\zeta(s)$), subdividing sections so that no interval is longer than h.
   - Adjust the initial condition ψ_t
   - Integrate forward & backward through the atmosphere to give r(s), θ(s) and ψ (s).
   - Use a straight line ray from just outside the atmosphere where n=1 to the satellite altitude to calculate the angle ψ_s by which the ray misses the instrument
   - Evaluate $\zeta(s)$ at each quadrature point (use r, ψ to interpolate in the 2-D profile table).
   until converged (fixed number of times, probably 3 or 4)

Carry out the path integrals using the same quadrature points and e.g. Simpsons rule.

The fixed number of iterations is required so that we safely can do a numerical perturbation of the ray trace for the Jacobian calculation.

A reasonable initial value for ψ_t can be obtained by starting with the highest tangent point required, initialized with the geometric (unrefracted) value, and work downwards, each time using the final value for the previous level as the initial value for the current level.

We should probably check for pathological circumstances such as the ray being refracted below the tangent level, by at least checking whether $r < r_t$! This applies to the homogeneous case too.

The alternative approach of finding the scan angle θ_s at the satellite which gives a tangent point at the right pressure level turns out to be more complicated, and not worth pursuing:

A3.3.1.1.7 The gas equation for air

The gas equation for air is given by Ciddor [1996] as

$$\rho = \frac{M_{dry}}{R^*T} p \cdot \frac{\left[1 - X_{H_2O}\left(1 - \frac{M_{H_2O}}{M_{dry}}\right)\right]}{Y}, \qquad (A2.32)$$

where $R^* = 8.31451$ J mole^{-1} K^{-1}, the universal gas constant;

$M_{dry} = [28.9635 + 12.011*10^{-6}(X_{CO2} - 400)]*10^{-3}$ kg/mole;

$X_{CO2} = 1.5202 * q_{CO2}$;

$M_{H2O} = 0.018015$ kg/mole;

$X_{H2O} = 0.6223 * q_{H2O}$; and

the compressibility factor Y is given by

$Y = 1 - (P/T)[a_0 + a_1t + a^2t^2 + (b_0 + b_1t)X_{H2O} + (c_0 + c_1t)X_{H2O}^2] + (P/T)^2(d + eX_{H2O}^2)$

where
$a_0 = 1.58123e^{-6}$
$a_1 = 2.9331e^{-8}$
$a_2 = 1.1043e^{-10}$
$b_0 = 5.707e^{-6}$
$b_1 = 2.051e^{-8}$
$c_0 = 1.9898e^{-4}$
$c_1 = 2.376e^{-6}$
$d = 1.83e^{-11}$
$e = -0.765e^{-8}$
and t = T-273.15

A3.3.1.1.8 Refractive index of air

The index of refraction of air (n) depends on frequency (v), pressure (P), temperature (T) and water vapor amount (partial pressure P_{H2O}). Since the original Edlén equation was published in the early 1960's [Edlén, 1966], many revised empirical formulas have been published based on the new measurements. We use a revision of Edlén by Birch and Downs [1993 and 1994]:

$$n = n_{tp} - f \cdot \left(a_9 - a_{10} v^2 \right) \cdot 10^{-10};$$

$$n_{tp} - 1 = \frac{P(n_s - 1)}{a_5} \cdot \frac{\left[1 + 10^{-8} \left(a_6 - a_7 t \right) P \right]}{\left(1 + a_8 t \right)}; \text{and} \qquad (A2.33)$$

$$(n_s - 1) \cdot 10^{-8} = a_0 + a_1 \cdot \left(a_2 - v^2 \right)^{-1} + a_3 \left(a_4 - v^2 \right)^{-1};$$

where a_0 to a_{10} are constants (a_0 = 8342.54; a_1 = 2406147.0; a_2 = 130.0; a_3 = 15998.0; a_4 = 38.9; a_5 = 96095.43; a_6 = 0.601; a_7 = 0.00972; a_8 = 0.003661; a_9 = 3.7345; a_{10} = 0.0401;), v is frequency in mm^{-1}, P is pressure in Pa, t is temperature in °C ($t = T$ -273.15), and f is the partial pressure of water vapor.

Although the above formula was derived from measurements of visible and near infrared region, other measurements suggest that it could be extrapolated to the infrared region [Coleman *et al.,* U.S. NBS, "Table of Wavenumbers", 1960]. Note that frequency (v) only has a secondary effect on n, so that the ray-trace step simply uses the averaged frequency for the forward model spectrum range in the calculation.

A3.3.1.5: Non-LTE

The single-line volumetric absorption κ_v and local thermal radiance R_v is given by

$$\kappa_v = \frac{h\nu}{4}\ \overline{B}\left(g_u\,n_1 - g_1 n_u\right)\phi_v \qquad\qquad (A3.1)$$

and

$$R_v = \frac{h^2\nu^4}{2\pi c^2}\ g_1\,n_u\,\chi_v, \qquad\qquad (A3.2)$$

where

$$\chi_v = \phi_v\ e^{-h(v-v_o)/kT}, \qquad\qquad (A3.3)$$

where n_l and n_u are the number density populations of the lower and upper V-R states and the constant integers g_l and g_u, are the respective single state degeneracy factors.

This result is a general one for a two-level system. The lineshapes, χ_v and ϕ_v, are functions of the bulk thermodynamic quantities such as pressure, temperature, plus individual gas densities which can separately influence the far wing lineshapes. The populations are given by the Boltzman distribution <u>only</u> under conditions of local thermodynamic equilibrium. In the presence of a strong radiation field, or under conditions for which the relaxation rates are slow with respect to physical processes influencing the state populations, the upper and lower state populations are not simply related through Boltzmann factors associated with a characteristic temperature for the system and the source function for the radiance is no longer given by the Planck function.

In the present case for TES observations, several assumptions can be made which significantly simplify the Non-LTE problem: (1) the relevant transitions occur at low pressure so that the Doppler shape is dominant with the line shape for emission and absorption being the same; (2) the system is in translational equilibrium with a characteristic kinetic temperature (affects only the Doppler width); and (3) the system is in rotational equilibrium with a characteristic rotational temperature. In the present formulation, the Non-LTE radiative transfer is developed as an extension of the LTE radiative transfer minimizing complexity and computational cost. The Non-LTE vibrational state population variables can be used to relate the Non-LTE single-line absorption and radiance to the same quantities calculated for an atmosphere in equilibrium at the characteristic temperature $\overline{T}$. The relationship between non-equilibrium and equilibrium radiative properties for a single line can be summarized by

$$\kappa_v = \left[\frac{g_u n_1 - g_1 n_u}{g_u n_1^{\ e} - g_1 n_u^{\ e}}\right]\kappa_v^{\ e} \qquad\qquad (A3.3)$$

and

$$R_v = \frac{n_u}{n_u^{\ e}}\ R_v^{\ e}, \qquad\qquad (A3.4)$$

which can also be written in terms of the Planck function as

$$R_v = \frac{n_u}{n_u^{\,e}} \, B_v\left(\overline{T}\right) \kappa_v^{\,e}. \tag{A3.5}$$

The superscript e denotes the equilibrium values of the respective quantities.

The ratios of non-LTE vibrational populations to their equilibrium values are given as enhancement (or depletion) ratios,

$$r_1 = \frac{n_1}{n_1^{\,e}} \quad \text{and} \quad r_u = \frac{n_u}{n_u^{\,e}} \; . \tag{A3.6}$$

The single-line contributions to K_v and C_v due to a transition with wavenumber value v_o can be expressed simply in terms of these ratios according to

$$\kappa_v = \left[\frac{r_1 - r_u \, \Delta}{1 - \Delta} \right] \kappa_v^{\,e} \tag{A3.7}$$

and

$$C_v = \left[\frac{r_1 - r_u}{1 - \Delta} \right] K_v^{\,e} \tag{A3.8}$$

where Δ is the Boltzman factor,

$$\Delta = \frac{g_1 \, n_u^{\,e}}{g_u \, n_1^{\,e}} = e^{-h v_o / k \overline{T}}. \tag{A3.9}$$

The factors in brackets can be viewed as Non-LTE line strength correction factors. The functions, K_v and C_v, are obtained from the equilibrium values of the spectral absorption coefficients tabulated for individual vibrational states of a given molecular species. The quantities required for the calculation are r_1, r_u and v_o for each Non-LTE vibrational state.

The complete solution of the radiative transfer equation for a homogeneous path is given by

$$L_v = L_v^{\,o} \, e^{-\kappa_v u} + B_v\left(\overline{T}\right) \left[1 - \frac{C_v}{\kappa_v} \right] \left[1 - e^{-\kappa_v u} \right] \tag{A3.10}$$

where $L_v^{\,o}$ is the radiation at the path boundary. The effect of solving the non-equilibrium problem for a homogeneous layer is effectively to modify the line strengths (equilibrium absorption coefficients) contributing to the local absorption coefficient K_v, and to replace the Planck function B_v by the high resolution function $B_v\left(\overline{T}\right) \left[1 - C_v / K_v \right]$.

A3.3.2.2: Map of Earth Surface Composition

Global Land Cover Characteristics Data Base

This appendix describes an existing source of global land cover maps with 1 km resolution and a choice of land classification schemes. This database was generated by the U.S. Geological Survey (USGS) Earth Resources Observation System (EROS) Data Center, the University of Nebraska-Lincoln (UNL) and the Joint Research Centre of the European Commission and is described in more detail at: http://edcwww.cr.usgs.gov/landdaac/glcc/glcc.html. Their maps are derived primarily from 1 km resolution composites of normalized difference vegetation index (NDVI) data from the Advanced Very High Resolution Radiometer (AVHRR) for the 12 month period of April 1992-March 1993. (NDVI values are the difference divided by the sum of the near infrared (channel 2) and visible (channel 1) reflectance values, after calibration and atmospheric corrections).The strategy for global land cover characterization is given in Loveland *et al* [1991, 1995] and Brown *et al*[1993] and an AVHRR data quality evaluation is described in Zhu and Yang [1996].The global land cover maps are available in 6 different classifications schemes with a range of 10 to 94 land cover types. These schemes are optimized to provide relevant information for research in areas such as atmospheric general circulation models and land use studies. Three of these classification schemes include urban/built-up areas as a land cover type, a useful distinction for our purposes. These are the Global Ecosystems classification (94 classes), Olson [1994 a&b]; the USGS Land Use/Land Cover System (24 classes), Anderson *et al* [1976]; and the International Geosphere Biosphere Programme (IGBP) Land Cover Classification (17 classes), Belward [1996]. Although we should not preclude the use of the more detailed Global Ecosystems classification, the USGS Land Use/Land Cover system (listed below) has been chosen for the initial algorithm development. The IGBP scheme, although simpler, was not chosen because there were no classes to distinguish moist vs. dry vegetation, an important distinction because of significant spectral IR reflectance differences. None of the land cover classifications in this database distinguished ice from snow, and an additional database may be needed for these areas.

Table A - 1: USGS Land Use/Land Cover System Legend (Modified Level 2)

Value	Code	Description
1	100	Urban and Built-Up Land
2	211	Dryland Cropland and Pasture
3	212	Irrigated Cropland and Pasture
4	213	Mixed Dryland/Irrigated Cropland and Pasture
5	280	Cropland/Grassland Mosaic
6	290	Cropland/Woodland Mosaic
7	311	Grassland
8	321	Shrubland
9	330	Mixed Shrubland/Grassland
10	332	Savanna
11	411	Deciduous Broadleaf Forest
12	412	Deciduous Needleleaf Forest
13	421	Evergreen Broadleaf Forest
14	422	Evergreen Needleleaf Forest
15	430	Mixed Forest
16	500	Water Bodies
17	620	Herbaceous Wetland
18	610	Wooded Wetland
19	770	Barren or Sparsely Vegetated
20	820	Herbaceous Tundra
21	810	Wooded Tundra
22	850	Mixed Tundra
23	830	Bare Ground Tundra
24	900	Snow or Ice

A3.4: Jacobians

The radiance at the satellite in terms of component contributions from the atmosphere and the surface, but neglecting the solar contribution, may be written as,

$$L_{sat} = L_L^{\uparrow} + \left[\varepsilon B\left(T_{sfc}\right) + \alpha L_0^{\downarrow} \right] T_{0,L} \tag{A4.1}$$

in which $L_L^{\uparrow}$ is the upwelling radiance contribution of the atmosphere from the surface to the level at the top of the atmosphere (TOA), $T_{0,L}$ is the transmittance of the atmosphere and $L_0^{\downarrow}$ is the downwelling radiance at the surface. For a specularly reflecting surface, $L_0^{\downarrow}$ is calculated for the same zenith angle as $L_L^{\uparrow}$ and α is the appropriate bidirectional reflectance. For a Lambertian surface, $L_0^{\downarrow}$ is calculated at the diffusivity angle, the downwelling radiation scattered by the surface is taken to be isotropic and α is the albedo.

Due to the form of the radiative transfer equation, the analytic derivative of the radiance at the satellite with respect to a change in parameter x_l at level l, is most expeditiously obtained in terms of associated layer quantities, so that we have

$$\frac{\partial L_{sat}}{\partial x_l} = \sum_j \frac{\partial L_{sat}}{\partial \overline{x}_j} \frac{\partial \overline{x}_j}{\partial x_l} \tag{A4.2}$$

in which x_l is an element of the retrieval vector associated with level l and $\overline{x}_j$ is the associated layer quantity for layer j. Note that in general, x may be mixing ratio (log mixing ratio) or temperature in this context.

In this section we focus on the computation of $\dfrac{\partial L_{sat}}{\partial \overline{x}_j}$, noting that $\dfrac{\partial \overline{x}_j}{\partial x_l}$ is independent of wavenumber. Differentiating Eq. A4.1 with respect to $\overline{x}_j$ we obtain

$$\frac{\partial L_{sat}}{\partial \overline{x}_j} = \frac{\partial L^{\uparrow}}{\partial \overline{x}_j} + \varepsilon B\left(T_{sfc}\right) \frac{\partial T_{0,L}}{\partial \overline{x}_j} + \alpha \frac{\partial L_0^{\downarrow}}{\partial \overline{x}_j} T_{0,L} + \alpha L_0^{\downarrow} \frac{\partial T_{0,L}}{\partial \overline{x}_j} \tag{A4.3}$$

$$= \frac{\partial L^{\uparrow}}{\partial \overline{x}_j} + \alpha T_{0,L} \frac{\partial L_0^{\downarrow}}{\partial \overline{x}_j} + \left[\varepsilon B\left(T_{sfc}\right) + \alpha L_0^{\downarrow} \right] \frac{\partial T_{0,L}}{\partial \overline{x}_j} \tag{A4.4}$$

It will prove useful to consider the partial derivative of the total transmittance with respect to the layer optical depth, $\dfrac{\partial T_{0,L}}{\partial \tau_j}$, which can be written as

$$\frac{\partial T_{0,L}}{\partial \tau_j} = \frac{\partial \{T_l \mathrm{L}\ T_j \mathrm{L}\ T_L\}}{\partial T_j} \tag{A4.5}$$

$$= \frac{\partial \{\exp(-\tau_1)\mathrm{L}\ \exp(-\tau_j)\mathrm{L}\ \exp(-\tau_L)\}}{\partial T_j} \tag{A4.6}$$

$$= \{\exp(-\tau_1)\mathrm{L}\ [-\exp(-\tau_j)]\mathrm{L}\ \exp(-\tau_L)\} \tag{A4.7}$$

$$= -T_{0,L} \tag{A4.8}$$

Thus we have the simple result that the partial derivative of the total transmittance with respect to the optical depth in any layer is the negative of the total transmittance.

We proceed next to consider the partial derivative of the total transmittance with respect to layer mixing ratios,

$$\frac{\partial T_{0,L}}{\partial \overline{q}_{l,m}} = \frac{\partial T_{0,L}}{\partial \tau_l}\ \frac{\partial \tau_l}{\partial \overline{q}_{l,m}} \tag{A4.9}$$

where $\overline{q}_l$ is the layer mean mixing ratio for molecule m in layer l. The optical depth can be written as follows

$$\tau_l(\overline{T}_l) = \sum_m u_{l,m} \kappa_{l,m}(\overline{T}_l) + u_{l,1} \left\{ C_f(\overline{T}_l)\left(\frac{\overline{\rho}_{l,dry}}{\rho_0}\right) + C_s(\overline{T}_l)\left(\frac{\overline{\rho}_{l,1}}{\rho_0}\right) \right\} \tag{A4.10}$$

where $\overline{T}_l$ is the layer mean temperature, $\kappa_{l,m}$ is the absorption coefficient for molecule m and u_m is the integrated path amount for molecule m. For the purposes of this derivation, the air broadened continua contributions are considered as included in $\kappa_{l,m}$. The self broadened water vapor continuum contribution is given explicitly in terms of the continuum coefficient $C_s(\overline{T}_l)$ with $\overline{\rho}_{l,1}$ the number density of water vapor in layer l and ρ_0 the reference number density with $P_0 = 1$ atm and $T_0 = 296$ K. Eq. A4.10 may be written in terms of layer mixing ratio as

$$\tau_l(T_l) = u_l \left\{ \sum_m \overline{q}_{l,m} \kappa_{l,m}(\overline{T}_l) + C_f(\overline{T}_l)(1-\overline{q}_{l,1})\left(\frac{\overline{\rho}_l}{\rho_0}\right) + C_s(\overline{T}_l)\overline{q}_{l,1}\left(\frac{\overline{\rho}_l}{\rho_0}\right) \right\} \tag{A4.11.1}$$

$$= u_l \left\{ \sum_m \overline{q}_{l,m} \kappa_{l,m}(\overline{T}_l) + \overline{q}_{l,1}\left(\frac{\overline{\rho}_l}{\rho_0}\right)\left[C_f(\overline{T}_l) + \overline{q}_{l,1}\left[C_s(\overline{T}_l) - C_f(\overline{T}_l) \right] \right] \right\} \tag{A4.11.2}$$

$$= u_l\ \overline{\kappa}_l \tag{A4.12}$$

where $\bar{\rho}_l$ is now the mean number density for the layer and u_l is the integrated path amount for dry air in the layer. The effective absorption coefficient, $\bar{\kappa}_l$, will be prove useful in the subsequent development. From Eq. A4.9, the partial derivative of the total transmittance with respect to layer mixing ratio in layer l can now be obtained as

$$\left. \frac{\partial T_{0,L}}{\partial \bar{q}_{l,m}} \right|_{m \neq 1} = -T_{0,L} \left\{ u_l \kappa_{l,m} \left(\bar{T}_l \right) \right\} \qquad (A4.13.1)$$

and

$$\frac{\partial T_{0,L}}{\partial \bar{q}_{l,1}} = -T_{0,L} \left\{ u_l \left[\kappa_{l,1} \left(\bar{T}_l \right) + 2\bar{q}_{l,1} C_s \left(\bar{T}_l \right) \left(\frac{\bar{\rho}_l}{\rho_0} \right) \right] + \frac{\partial u_l}{\partial \bar{q}_{l,1}} \bar{\kappa}_l \right\} \qquad (A4.13.2)$$

In this derivation the explicit dependence of the self-continuum due to water vapor has been included because of its large contribution to the radiance in the boundary layer and lower troposphere. The layer pressure boundaries are assumed constant for these derivatives with the implicit constraint that the mass in the layer be constant and thus the column of dry air must increase as the mixing ratio of water vapor in the layer is increased, the second term in Eq. A4.13.2. The change in the dry air column due to changes in mixing ratios of the other species being retrieved is negligible. The magnitude of this term should be assessed to establish whether implementation is necessary in the computation of the derivatives. The dependence of the optical depth on the self broadened line width of water vapor has not been included in the calculation of the derivative since its contribution to the radiance, though non-negligible, is small enough to neglect for present purposes. Eq. A4.13 thus provides the result for the last term in Eq. A4.4. Note that this expression is simple and contains terms that have been obtained in the course of the radiance calculation.

We now consider this same term for the case in which the elements of the retrieval vector are temperature, $\frac{\partial T_{0,L}}{\partial \bar{T}_l}$. We have from Eq. A4.9,

$$\frac{\partial T_{0,L}}{\partial \bar{T}_l} = \sum_{l'} \frac{\partial T_{0,L}}{\partial \tau_{l'}} \frac{\partial \tau_{l'}}{\partial \bar{T}_l} \qquad (A4.14)$$

$$= -T_{0,L} \left\{ \left. \frac{\partial \tau_l}{\partial \bar{T}_l} \right|_{u_l} + \sum_{l'} \bar{\kappa}_{l'} \frac{\partial u_{l'}}{\partial \bar{T}_l} \right\} \qquad (A4.15)$$

The first term in Eq. A4.15 is straightforward to implement for the case in which the absorption coefficients are tabulated as a function of temperature and is very efficient. In the current version of TWPR, three point Lagrange interpolation is used to obtain the optical depths at the specified layer temperature. The analytic derivative for this term is readily obtained from the interpolation expression. This result is one of the principal reasons for utilizing absorption

coefficient tables. The second term in Eq. A4.15 arises in the calculation of the integrated path amounts along the refracted path for the limb case. The layer mixing ratios are assumed to be constant for present purposes, a premise that needs to be confirmed. With some added complication, the effect of the variation of the column amounts with temperature can be included in the calculation of the optical depth at the three temperatures, facilitating the implementation of this contribution to the temperature derivative.

It should be noted that there are implications in this approach for the algorithms employed. For this case, it is desirable in calculating the radiative transfer, to obtain the spectral optical depths at the three appropriate temperatures and then to perform the interpolation to the layer temperature rather than interpolating the absorption coefficients to the layer temperature. For the partials with respect to mixing ratio, however, the absorption coefficients of the relevant species at the layer temperature are required (Eq. A4.13). Considerable acceleration can be achieved in this regard if derivatives with respect to temperature and mixing ratio are not required simultaneously. In general, this is not always possible nor necessarily desirable, but it does lead to computational saving. In addition, the algorithm should be developed to avoid computation of derivative components when they are small: when $T_{0,L}$ is small or for water vapor in certain spectral regions above a given altitude.

We now consider the other terms in Eq. A4.4. In considering the partial derivatives of the up and downwelling atmospheric radiance with respect to layer quantities, we adopt an algorithmic perspective to simplify the development and facilitate implementation. We utilize a simplified form of the radiative transfer equation ignoring the 'linear in τ' dependence on the Planck function. The contribution from this term is not large and may readily be included at a subsequent stage in the implementation.

The first step is to start at the TOA and calculate the optical depths (τ_l), layer transmittances (T_l) and total transmittance to each atmospheric level ($T_{l,L}$) in accordance with the following figure (Figure A-3) where and $T_{l-1,L}$ is obtained from $T_{l,L} \times T_l$ with $T_{L-1,L} \equiv 1$.

Figure A - 3: First Step in Jacobians
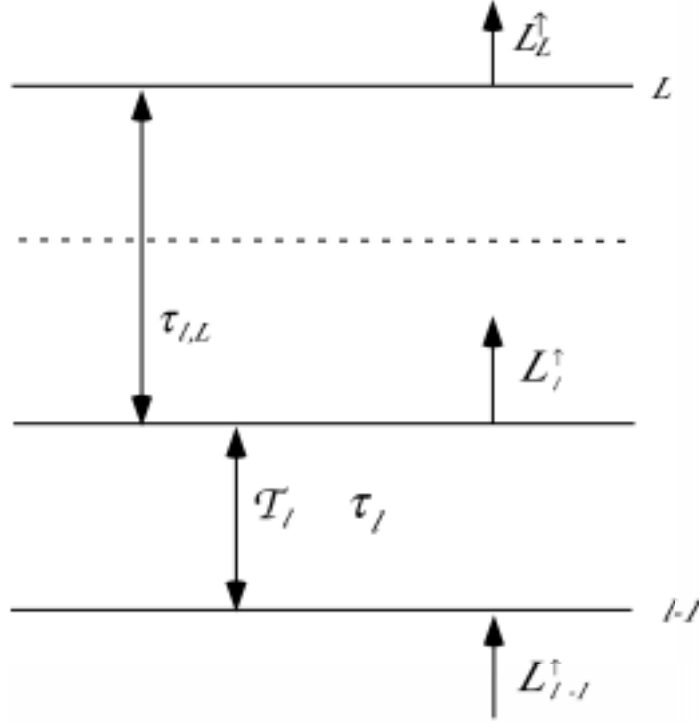
If at some level L_{min}, $T_{L_{min},L}$ is below a preset threshold, then L_{min} becomes the lowest level that must be treated in the entire problem and the Eq. (A4.1) becomes

$$L_{sat} = L_L^\uparrow \tag{A4.16}$$

so that the surface and the downwelling contributions may be ignored. If $T_{l,L}$ does not go below the threshold, then $L_{min} = 0$ and all terms of Eq. A4.1 must be considered.

The second step in obtaining $L_{sat}^\uparrow$ and the relevant derivatives is to consider the radiative transfer algorithm initialized at L_{min} and proceeding to level L. The radiance at level l is given by

$$L_l^\uparrow = T_l L_{l-1}^\uparrow + B\left(\overline{T}_l\right)\left(1 - T_l\right) \tag{A4.17}$$

with $L_{L_{min}}^\uparrow = 0$.

At a given stage in the calculation we can write $L_L^\uparrow$ as the sum of the two terms,

$$L_L^\uparrow = L_l^\uparrow T_{l,L} + L_{l,L}^\uparrow \tag{A4.18}$$

in which $L_{L,l}^{\uparrow}$ is the contribution to the radiance from layers above layer l (level l). Substituting Eq. A4.17 into Eq. A4.18, we obtain

$$L_{L}^{\uparrow} = \left\{ T_l\, c + B(\overline{T_l})(1 - T_l) \right\} T_{l,L} + L_{l,L}^{\uparrow} \qquad (A4.19)$$

It is important to note that $L_{l-1}^{\uparrow}$ and $L_{l,L}^{\uparrow}$ do not contain any dependence with respect to layer quantities associated with layer l. Thus, this form is particularly useful for the evaluation of the derivative with respect to the general layer quantity $\overline{x}_l$,

$$\frac{\partial L_{L}^{\uparrow}}{\partial \overline{x}_l} = \left\{ \frac{\partial T_l}{\partial \overline{x}_l} L_{l-1}^{\uparrow} + \frac{\partial B(\overline{T_l})}{\partial \overline{x}_l}(1 - T_l) - B(\overline{T_l})\frac{\partial T_l}{\partial \overline{x}_l} \right\} T_{l,L} \qquad (A4.20)$$

This expression includes the effect of $\overline{x}_l$ on attenuating the incoming radiation to the layer as well as on the radiance originating in the layer.

We next consider the case in which $\overline{x}_l$ is the mixing ratio associated with molecule m. Taking advantage of the expressions previously derived we obtain

$$\frac{\partial L_{L}^{\uparrow}}{\partial \overline{x}_{l,m}} = \left\{ \frac{\partial T_l}{\partial \tau_l}\frac{\partial \tau_l}{\partial \overline{x}_{l,m}}\left[L_{l-1}^{\uparrow} - B(\overline{T_l}) \right] \right\} T_{l,L} \qquad (A4.21)$$

$$= \left\{ \left[B(\overline{T}) - L_{l-1}^{\uparrow} \right] T_l \frac{\partial \tau_l}{\partial \overline{x}_{l,m}} \right\} T_{l,L} \qquad (A4.22)$$

Note that all quantities required here have previously been calculated so that this contribution to the partial derivatives may be evaluated at each step in the algorithm. The partial derivative of optical depth with respect to mixing ratio may be obtained from the bracketed terms in Eqs. A4.13.1 and A4.13.2.

Next consider the derivative of $L_{L}^{\uparrow}$ with respect to layer temperature,

$$\frac{\partial L_{L}^{\uparrow}}{\partial \overline{T}_L} = \left\{ \frac{\partial T_l}{\partial \overline{T}_l} L_{l-1}^{\uparrow} + \frac{\partial B(\overline{T_l})}{\partial \overline{T}_l}(1 - T_l) - B(\overline{T_l})\frac{\partial T_l}{\partial \overline{T}_l} \right\} T_{l,L} \qquad (A4.23)$$

$$= \left\{ \frac{\partial T}{\partial \tau_l}\frac{\partial \tau_l}{\partial \overline{T}_l}\left[L_{l-1}^{\uparrow} - B(\overline{T_l}) \right] + \frac{\partial B(\overline{T_l})}{\partial \overline{T}_l}(1 - T_l) \right\} T_{l,L} \qquad (A4.24)$$

$$= \left\{ \left[B(\bar{T}_l) - L^{\uparrow}_{l-1} \right] T_l \frac{\partial \tau_l}{\partial \bar{\bar{T}}_l} + \frac{\partial B(\bar{T}_l)}{\partial \bar{T}_l} (1 - T_l) \right\} T_{l,L} \qquad \text{(A4.25)}$$

Again, all terms are available, with the previous discussion of $\dfrac{\partial \tau_l}{\partial \bar{T}_l}$ applicable in this case as well.

The derivative of the Planck function with respect to layer temperature is calculated and stored using a piecewise linear update as is used for the Planck function. Also note that many of the terms are just those required for the radiative transfer calculation itself, Eq. A4.3.17.

Finally consider the second term in Eq. A4.4 in which $\dfrac{\partial L^{\downarrow}_0}{\partial \bar{x}_j}$ is required. Recall this term is only

necessary if $L_{\min} = 0$. This case is essentially identical to that required for $\dfrac{\partial L^{\uparrow}_L}{\partial \bar{x}_j}$ except that the

direction is reversed. The transmittance from the surface to each successive level is required, $T_{0,l}$, readily obtained since the T_l have been saved. The radiance calculation is initiated at level L (TOA) and proceeds to level 0 (sfc). Note that the integrated path amounts and the layer transmittances may be different from those used for $L^{\uparrow}_L$ depending on whether the surface is Lambertian or specular.

The extension of the present approach to the limb viewing case is straightforward. The emissivity, ε, in the present formulation is set to zero and the albedo, α, is set to unity. This approach enables the treatment of atmospheres that are asymmetric about the line of sight tangent point with minimal additional effort. A critical remaining task is the development of the partial derivatives of the layer quantities with respect to level quantities. This can be achieved by developing the necessary analytic derivatives where feasible. For variables for which this is difficult, the finite difference approach may be utilized. In the course of implementing the coding for the analytic derivatives, validation using the currently implemented finite difference method will be essential. In this development for the analytic derivatives, the solar contribution has been neglected for simplicity of exposition. Inclusion of this contribution is straightforward in the context of the present formulation. It should be emphasized that the derivation is most directly obtained for the variable associated with species profile taken as volume mixing ratio, $\bar{q}_m$. If another variable is preferred, e.g., log $\bar{q}_m$, this variable change can be made as part of the transformation from layer to level quantities. A final point with respect to the transformation from level quantities to layer quantities, is the fact that the transformation is not dependent on frequency. Consequently, this transformation may be performed after the spectral convolution is performed, providing a potential saving of time and providing an opportunity for increased flexibility in the retrieval vector definitions without significantly impacting computational cost.

A3.3.8.1: Line Parameters: ABSCO Databases

H_2O (molecule 1)

There are numerous, significant deficiencies in the currently available water vapor parameters in the thermal IR spectral region covered by TES. A major update to the positions, intensities, air-broadening coefficients, self-broadening coefficients, and pressure-induced shifts is in preparation (R. A. Toth, Jet Propulsion Laboratory, private communication, 1998).

As was done for the ATMOS compilation [Brown *et al.,* 1995], we plan to treat HDO and a separate molecular species because of the large fractionation effects of HDO with respect to H_2O. The current database does not include the updated positions and intensities of the $HD^{16}O$ v_2 band derived by Flaud *et al.* [1986] and the more recent v_2 $HD^{16}O$, $HD^{17}O$, and $HD^{18}O$ position and intensity analysis results of Toth [1993]. The parameters of Flaud *et al.* [1986] have been regenerated (J.-M. Flaud, private communication) and are now available to the TES project with approximate air-broadened widths (C. P. Rinsland, private communication, 1998). Air-broadened pressure shifts are set to zero.

CO_2 (molecule 2)

A new global least-squares fit of the energy levels of carbon dioxide is performed for each edition of HITRAN to improve the accuracy [Rothman *et al.,* 1998]. In addition, absolute intensities are computed from an updated set for each edition. Recent studies not yet incorporated in the HITRAN global fit include the analysis of 1500 lines in 36 vibration-rotation bands of $^{12}C^{16}O_2$ between 3090 and 3850 cm^{-1} [Malathy Devi *et al.,* 1998a]. The results were derived from room temperature 0.01- cm^{-1} resolution laboratory spectra recorded at Kitt Peak. Although this spectral region will not measured by TES, the line positions will improve the $^{12}CO_2$ energy levels for future HITRAN updates. Recent developments in the infrared spectroscopy of CO_2 have been reviewed by Malathy Devi *et al.* [1996].

O_3 (molecule 3)

Updates for O_3 on the 1996 HITRAN compilation and updates not incorporated in the current edition of HITRAN have been summarized by Rinsland *et al.* [1998a]. There are several results of importance for TES studies.

Spectra of ^{17}O-enriched ozone samples have been recorded at 0.005-cm^{-1} resolution and analyzed to derive the line positions and intensities for the v_1 and v_3 bands of $^{16}O^{17}O^{16}O$ [Heyart *et al.,* 1992] and $^{16}O^{16}O^{17}O$ [Heyart *et al.,* 1993]. As described by Rinsland *et al.* [1998a], these parameters, which are not included on HITRAN 1996 [Rothman *et al.,* 1998] have been used to identify isolated lines of the v_3 bands of $^{16}O^{17}O^{16}O$ and $^{16}O^{16}O^{17}O$ in both high resolution ground-based and balloon-borne stratospheric solar absorption spectra. Hence, they may be detectable in TES spectra and will need to be included for accurate retrievals.

 The first high-resolution analysis of the $v_1 + v_3$ bands of $^{16}O^{16}O^{18}O$ and $^{16}O^{18}O^{16}O$ at 4.8 μm was performed by Flaud *et al.* [1994]. On the basis of that work, isolated lines of both heavy isotopic

species have been identified in high resolution ground-based solar absorption spectra by Arlander et al. [1994] and Goldman et al. [1998] and in high resolution stratospheric solar occultation spectra by Goldman et al.[41] At the present time, the potential use of these lines for quantitative atmospheric studies has not been fully realized. The levels of the (101) vibrational upper state are perturbed by interactions with the nearby, unobserved rotational levels of the (002) and (200) states.[39] Positions and relative intensities computed for unperturbed lines have been used to identify suitable intervals for future quantitative ^{18}O-isotopic ozone atmospheric studies.[41]

Absolute intensities of 376 $^{16}O_3$ lines in the 9-11 μm region have been measured from room temperature spectra recorded at 0.0027-cm^{-1} with the National Solar Observatory facility on Kitt Peak [Smith et al., 1998]. The ozone samples were contained in a glass cell having crossed IR-transmitting and UV-transmitting paths approximately 10 cm in each direction. The ozone partial pressures were determined in the cell were determined from measurements of the 254-nm UV absorption using the absorption cross sections of Mauersberger et al. [1987] as the reference standard. A multispectrum nonlinear least-squares fitting technique was used to determine the intensities of 366 lines in the P, Q, and R branches of the v_3 fudamental and 10 lines in the R branch of the v_1 band. The absolute accuracies of the lines ranged from 2% for the strongest, most well-determined lines to 4 to 5% for the weakest lines measured. On average, the measured intensities are 1% larger than he values on the 1996 HITRAN list [Rothman et al., 1998]. This result indicates that the intensity scale assumed for HITRAN O_3 at 10 μm is sufficiently accurate for retrievals of O_3 from the TES observations.

CO (molecule 5)

Self-broadening and self-shift coefficients have been measured recently in the fundamental band of $^{12}C^{16}O$ [Malathy Devi et al., 1998b]. The results were obtained by analyzing five 0.0027- cm^{-1} resolution room temperature laboratory spectra simultaneously using a multispectrum nonlinear least-squares fitting technique. The self-broadening coefficients are lower than on HITRAN 1996 [Rothman et al., 1998] whereas the self-shifts are different in the P and R branches at the same *m* with values that range from +0.0005(1) to -0.0042(3) cm^{-1}atm^{-1} at 296 K. A laboratory study to measure the broadening and the shifts of CO in air at room and low temperatures is planned for the new future (M. A. H. Smith, private communication, 1998).

CH_4 (molecule 6)

The ongoing work summarized in the CH4 section of the HITRAN 1996 main paper (Rothman et al., 1998) is essential for a number of TES objectives.

NO_2 (molecule 10)

Perrin et al. [1998] have reviewed the status of NO_2 line parameters. Below is a summary of the important problems that are likely to affect TES retrievals based on that review and other recent studies.

The 3.4 μm region corresponds to the $v_1 + v_3$ band and the associated first hot band $v_1 + v_2 + v_3 - v_2$. Although 20 times weaker than the absorption in the 6.2 μm region, the 3.4 μm bands occur in a window region that can be measured in nadir spectra. Recently, a new analysis for positions and intensities has been performed from Fourier transform spectra [Mandin *et al.,* 1997]. The analysis took into account both the Coriolis interaction between the spin-rotation levels of the (101) vibrational state and those of (120) and the spin-rotation resonances within (101) and (120). Although the experimental intensities of the $v_1 + v_3$ band lines are in good agreement with earlier work, the hot band lines are about 1.48 times lower than determined previously [Perrin *et al.,* 1982].

In HITRAN 1996 [Rothman *et al.,* 1998], the air-broadening coefficients are set to 0.067 cm^{-1}atm^{-1} at 296 K for all lines, except for the 3.4 μm region, where the air-broadening coefficients for all lines are set to 0.063 cm^{-1}atm^{-1} at 296 K. However, as described below there is evidence for a need to update the HITRAN air-broadening values.

Dana *et al.* [1997] have reported self-, N_2-, and O_2-broadening coefficients of NO_2 lines in the $v_1 + v_3$ band at 3.4 μm. The study found a slight rotational dependence of the broadening coefficients versus N", whereas no significant dependence was observed versus K_a". An empirical relation was derived to compute air-broadening coefficients at 296 K with an uncertainty of about "10% for values of N" and K_a" less than 40 and 10, respectively. The authors note that for typical lines used for atmospheric applications, the single value reported in the HITRAN database for all lines of all bands of NO_2 can differ by more than 20% from the measured values [Dana *et al.,* 1997]. A preliminary analysis of unpublished spectra of the 1600 cm^{-1} NO_2 band indicates that the widths of these lines are also too small in the HITRAN linelists with tests indicating that the changes produce a 10% increase in the retrieved mixing ratio of NO_2 at 25 km and little effect above 30 km [Sen *et al.,* 1998].

HNO_3 (molecule 12)

Recently, Perrin *et al.* [1998] have reanalyzed the $v_8 + v_9$ band at 1205 cm^{-1} based on a 0.003-cm^{-1} resolution laboratory spectrum recorded at the University of Denver. As in a recent analysis [Wang *et al.,* 1997], the Hamiltonian for fitting the line positions takes into account the ÄK " 2 anharmonic resonance linking the rotational levels of the $v_8=1$, $v_9=1$ "bright" vibrational state with those of the $v_7=1$, $v_8=1$ "dark" vibrational state. However, in contrast to previous work, $v_8 + v_9$ is noted to be a hybrid-type band with clearly identified B-type transitions among those of the strong A-type lines. The A- and B-type components of the transition moment operator of the , $v_8 + v_9$ band were determined through a least-squares fit of experimental line intensities measured from the spectrum. The new analysis extends the assignments for the , $v_8 + v_9$ band to maximum rotational quantum numbers of J=74 and K_a=49 as compared to a maximum J value of 57 [Wang *et al.,* 1997].

C_2H_6 (molecule 27)

Recently, assignments, improved positions, intensities, and air-broadening coefficients and their temperature dependence have been derived for the strong and sharp $^PQ_3$ subbranch of the v_7 band at 2976.8 cm^{-1} [Pine and Stone; 1996; Rinsland *et al.,* 1998; Pine and Rinsland, 1998]. This strong and sharp feature is prominent in ground-based solar spectra [Rinsland *et al.,* 1987; Rinsland *et al.,* 1998] and nearly free of atmospheric interferences. The new results were obtained from analysis of Doppler-limited and sub-Doppler molecular beam laboratory spectra . It may be possible to measure this C_2H_6 feature in the TES nadir view spectra.

COF_2 (molecule 29)

Although located almost entirely in the stratosphere, COF_2 produces IR absorption features in the limb spectra with absorptions located primarily in the regions of the v_1 (1944 cm^{-1}), v_4 (1243 cm^{-1}), and v_6 (774 cm^{-1}) bands. Recently, D'Cunha *et al.* [1997] have reported an analysis of the v_1 band region. The new analysis included the Fermi resonance with the $2v_2$ state and Coriolis interaction with the $2v_3 + v_6$ dark state. According to D'Cunha *et al.* [1997] , the results are in very good agreement with the values in HITRAN [Rothman *et al.,* 1998], as described by Rinsland *et al.* [1992]. Hence, we do not anticipate the need for a further update to the COF_2 parameters at this time.

Partition Functions

It is important to note that the partition functions supplied by HITRAN have several significant deficiencies as discussed by Goldman *et al.* [1998].

A3.3.8.2: Cross-Section P-T Interpolation Program XSFINT

1. **P-T Point outside table of temperature-pressure values**
   In this case the "distance" away from every point in the table is calculated and compared to find the closest point. The distance calculation is based on linear distance formulas where the pressure is divided by 10 to give similar units in temperature and pressure.

2. **P-T Point inside table of temperature-pressure values**
   This program picks points based on temperature lines where all temperatures within 2 degrees are considered to be on the same temperature line. A temperature line could look like

Temperature	Pressure
216	50.6
214.1	70.8
215.8	100.0

A table of pressures on temperature lines is constructed from which to pick points. There are four basic cases in the interpolate point outside table of temperature values; four points around target; three points around target; two points around target. The new cross-section records interpolated from the above cases are all written to a new cross-section file. The user can also select the points and interpolation method by hand rather than letting the program select the points and interpolation method.

Four points around target
   In this case 2 points on the temperature line before and after the target temperature are found where the points surround the target pressure.

   216.6,70.5   217.1,90.2 (temp line after)

   210.0,80.0 (target point)

   200.1,69.9   201.0,89.9   (temp line before)

   The corner pressures must be within 10% of each other (216.6,70.5 with 200.1,69.9 & 217.1,90.2 with 201.0,89.9) or the tightest diagonal line is picked and the 2 point temperature interpolate is activated, otherwise the 4 point interpolate is activated.

Three points around target
   In this case either the temperature line above or below the target contains only one point.

   216.6,70.5   217.1,90.2 (temp line after)
                   210.0,80.0 (target point)
   200.1,69.9   (temp line before)

   or

216.6,70.5   217.1,90.2 (temp line after)

210.0,80.0 (target point)

201.0,89.9   (temp line before)

If the target temperature is within 5 degrees of the temperature line with 2 points, then a 2 point pressure interpolate is activated between those two points. If the target temperature is not close enough to the temperature line with two points, then two points are chosen that create a diagonal (200.1,69.9 with 217.1,90.2 or 216.6,70.5 with 201.0,89.9) then the two point temperature interpolate is activated.

Two points around target
In this case one point on the temperature line before and after the target are used. If both points are either greater or smaller in pressure that the target, then the closest in pressure is used as the new point. If one of the two points are within 4% in temperature and 15% in pressure of the target, then that point is used as new point. If both points are within the 4% and 15% then the closest in temperature is used. If none of the above special cases occur then the 2 point temperature interpolate is activated.

Two point Temperature Interpolate
Two point temperature interpolate does a linear interpolate in temperature between the two pressure/temperature cross-section points for each point in the cross-sections.

Two point Pressure Interpolate
Two point pressure interpolate does a log interpolate in pressure between the two pressure/temperature cross-section points for each point in the cross-sections. (Note In the code the two point pressure interpolate is noted as a 3 point interpolate since two point temperature interpolate is noted as a 2 point interpolate)

Four point Interpolate
Four point interpolate does a linear interpolate in temperature between the side pressure/temperature cross-section points, then a log interpolate in pressure between the two new temperature points resulting from the linear temperature interpolate.

XSFINT Source Code

Xsfint has been compiled and tested on roma in /home/goldman/xsctions/interp. The source code for xsfint is all in one FORTRAN90 file called xsfint.F90. It contains two modules and one main code. The main code is at the end of the file, and must be there for it to use the two modules. The program has code to create plots using NCAR GKS graphics. The graphics code is currently disabled using conditional compilation with #define, #ifdef, #endif. All sections of graphics code are bracketed in #ifdef NCARGKSOUTPUT, #endif NCARGKSOUTPUT. The first line in the source code has a comment line

    !#define NCARGKSOUTPUT

Uncommenting this line, (removing the "!"), activates the graphics code. The source file is named with .F90 instead of .f90 to activate the pre-processor that processes the NCARGKSOUTPUT lines. To compile xsfint, activate f90 as follows

    f90 -o xsfint xsfint.F90

XSFINT Input
The input file format is as follows
        line1 -input cross-section filename
        line 2 -output cross-section filename
        line 3 -target temperature   target pressure interpolate select
                interpolate select
                0 = Automatic pick of points to interpolate and interpolate method
                1 = Use the temperature, pressure shown on line 4 to select a
        record from the cross-section file as the new point. (manual pick nearest
        point)
                2 = Use the temperature, pressure shown on line 4 and 5 to select 2
        records from the cross-section file to do a two point temperature interpolate
        on.
                3 = Use the temperature, pressure shown on line 4 and 5 to select 2
        records from the cross-section file to do a two point pressure interpolate on.
                4 = Use the temperature, pressure shown on line 4, 5, 6 and 7 to
        select 4 records from the cross-section file to do a four point interpolate on.

    Lines to specify manual selections contain
            temperature pressure
   There can be multiple target points selected in a run, each possibly with different
   interpolation selectors.
There is an example case on roma in /home/goldman/xsctions/interp and is named
cfc22.test.input. It contains
        ../cfc22.xsect   (cross-section file to read)
        cfc22.test.output   (cross-section file to create)
        220.0 50.0 3   (target 220.0,50.0 manual select points)
        216.0 176.8   (point 1 for 2 point pressure interp)
        216.0 40.9   (point 2 for 2 point pressure interp)
        240.0 300.0 0 (target 240.,300. auto select points & interp)
        226.0 223.0 2 (target 226.0, 223.0 manual select points)
        237.0 270.4   (point 1 for 2 point temperature interp)
        216.0 176.8   (point 2 for 2 point temperature interp)

Running XSFINT
To run xsfint on the test case on roma type
        xsfint <cfc22.test.input >& cfc22.test.output
This reads cfc22.test.input and creates cfc22.new.xsect and cfc22.test.output.

List of files

All files are on ms are in /GOLDMAN/VARANAS/XSEC.JUNE.97 except where noted
otherwise.

CCL4

Xsection file - ccl4.tar

Resolution - 0.03 cm^{-1}

Fixed 0.0025 cm^{-1} Spc file -ccl4.xsect.25

Avg Spc file - ccl4.xsect.avgspc
Table -   table.ME0216 in goldman output subdirectory
Number of Files   32
Wavenumber range   750.0100-811.9900 cm^{-1}

CFC11

Xsection file - cfc11.tar

Resolution - 0.01, 0.03 cm^{-1}

Fixed 0.0025 cm^{-1} Spc file -cfc11.xsect.A.25

cfc11.xsect.B.25

Avg Spc file - cfc11.xsect.avgspc.A

cfc11.xsect.avgspc.B
Table -   table.ME0131 (part a) in goldman output subdirectory
               table.ME7904 (part b) in goldman output subdirectory
Number of Files   55
Wavenumber range   810.0060-879.9930 cm^{-1}
                   1050.0000-1119.9930 cm^{-1}

CFC12

Xsection file - cfc12.tar

Resolution - 0.01, 0.02, 0.03 cm^{-1}
Fixed 0.0025 cm^{-1} Spc file -cfc12.xsect.A.25
cfc12.xsect.B.25

Avg Spc file - cfc12.xsect.avgspc.A
cfc12.xsect.avgspc.B
Table -   table.ME8745 (part a) in goldman output subdirectory
               table.ME6165 (part b) in goldman output subdirectory
Number of Files   51
Wavenumber range   850.0050-949.9950 cm^{-1}
                   1050.0060-1199.9850 cm^{-1}

CFC22

Xsection file - cfc22.tar
Resolution - 0.03 cm^{-1}
Fixed 0.0025 cm-1   Spc file -cfc22.xsect.25
Avg Spc file - cfc22.xsect.avgspc
Table -   table.ME0088 in goldman output subdirectory
Number of Files   7
Wavenumber range   760.0300-860.000 cm^{-1}

SF6

      Xsection file - sf6.tar

              Resolution -   0.03 cm^{-1}

      Fixed 0.0025 cm-1   Spc file -sf6.xsect.25

      Avg Spc file - sf6.xsect.avgspc

      Table -   table.ME0112 in goldman output subdirectory

      Number of Files   7

      Wavenumber range   925.0100-955.000 cm^{-1}

CF4

      Xsection file - cfc14.tar

              Resolution -   0.01, 0.03 cm^{-1}

      Fixed 0.0025 cm^{-1} Spc file -cfc14.xsect

      Avg Spc file - cfc14.xsect.avgspc

      Table -   table.ME0132 in goldman output subdirectory

      Number of Files   54

      Wavenumber range   1250.0050-1289.9975 cm^{-1}

REFERENCES

A3.3.1.1: Ray Tracing

Allen, C.W., *Astrophysical Quantities.* Athlone Press, 1976.

Ciddor, P.E. Refractive index of air: new equations for the visible and near infrared. *Applied Optics, 35,* 1566-1573, 1996.

Edlén, B., The Refractive Index of Air, *Metrologia, 2,* 71-80,1966.

Birch, K. P., and M. J. Downs, An Updated Edlén Equation for the Refractive Index of Air, *Metrologia, 30*, 155-162, 1993.

Birch, K. P., and M. J. Downs, Correction to the Updated Edlén Equation for the Refractive Index of Air, *Metrologia, 31*, 315-316, 1994.

Coleman, C. D., W. R. Bozman, and W. F. Meggers, *Table of Wavenumbers*, US Department of Commerce, NBS Monograph3, May, 1960.

A3.3.2.3: Global Land Cover Characteristics Data Base

Anderson, J.R., E.E. Hardy, J.T. Roach and R.E. Witmer, A land use and land cover classification system for use with remote sensor data, *U.S. Geological Survey Professional Paper 964,* 28, 1976.

Belward, A.S., ed., The IGBP-DIS global 1 km land cover data set (DISCover)-proposal and implementation plans, *IGBP-DIS Working Paper No. 13*, Toulouse, France, 1996.

Brown, J.F., T.R. Loveland, J.W. Merchant, B.C. Reed, and D.O. Ohlen, Using multisource data in global land cover characterization: concepts, requirements and methods, *Photogrammetric Engineering and Remote Sensing, 59,* 977-987, 1993.

Brown, J.F., B.C Reed, and L. Huewe, Advanced strategy for multi-source analysis and visualization in land cover characterization, *Proceedings, Pecora 13, Human Interactions with the Environment: Perspectives From Space,* in press.

Loveland, T.R., J.W. Merchant, J.F. Brown, D.O., Ohlen, B.C. Reed, P. Olson, and J.,Hutchinson, Seasonal land-cover regions of the United States, *Annals of the Association of American Geographers, 85,* 2, 339-355, 1995.

Loveland, T.R., J.W. Merchant, D.O. Ohlen, and J.F. Brown, Development of a land-cover characteristics database for the conterminous U.S., *Photogrammetric Engineering and Remote Sensing, 57*, 11, 1453-1463, 1991.

Loveland, T.R., D.O. Ohlen, J.F. Brown, B.C. Reed, Z. Zhu, J.W. Merchant, and L. Yang, Western hemisphere land cover-progress toward a global land cover characteristics database, *Proceedings, Pecora 13, Human Interventions with the Environment: Perspectives From Space,* in press.

Olson, J.S., 1994a, *Global ecosystem framework-definitions*, USGS EROS Data Center Internal Report, Sioux Falls, SD, 1994.

Olson, J.S., 1994b, *Global ecosystem framework-translation strategy*, USGS EROS Data Center Internal Report, Sioux Falls, SD, 1994.

Zhu, Z., and L. Yang, Characteristics of the 1-km AVHRR data set for North America, *International Journal of Remote Sensing, 17*, 1915-1924, 1996.

A3.3.8.1: ABSCO DATABASES: Line Parameters

Arlander, D. W., A. Barbe, M.T. Bourgeois, A. Hamdouni, J.-M. Flaud, C. Camy-Peyret, and Ph. Demoulin, The identification of $^{16}O^{18}O^{16}O$ and $^{16}O^{16}O^{18}O$ ozone isotopes in high resolution ground-based FTIR spectra, *J. Quant. Spectrosc. & Radiat. Transfer*, 52, 267-271, 1994.

Brown, L. R., M.R. Gunson, R.A. Toth, F.W. Irion, C.P. Rinsland and A. Goldman, The 1995 Atmospheric Trace Molecule Spectroscopy (ATMOS) Linelist. *Appl. Opt.*, 35, 2828-2848, 1996.

Dana, V., J.-Y. Mandin, M.Y. Allout, A. Perrin, L. Régalia, A. Barbe,J.-J. Plateaux and X. Thomas, Broadening parameters of NO_2 Lines in the 3.4 μm Spectral Region, *J. Quant. Spectrosc. Radiat. Transfer*, 57, 445-457, 1997.

D'Cunha, R., V.A. Job, G. Rahappan, V. Malathy Devi, W.J. Lafferty, and A. Weber, The High-Resolution Infrared Spectrum of the $v_1/2v_2$ Fermi Dyad Bands of COF_2, *J. Molec. Spectrosc.*, 186, 363-373, 1997.

Flaud, J.-M., C. Camy-Peyret, A. Mahmoudi, and G. Guelachvili, The v_2 band of $HD^{16}O$, Internat. *J. Infrared and Millimeter Waves*, 7, 1063-1090, 1986.

Flaud, J.-M., M.T. Bougeois, A. Barbe,J.J. Plateaux, and C. Camy-Peyret, The $v_1 + v_3$ bands of $^{16}O^{18}O^{16}O$ and $^{16}O^{16}O^{18}O$, *J. Molec. Spectrosc.*, 165, 464-469, 1994.

Goldman, A., W.G.Schoenfeld, T.M. Stephen, F.J. Murcray, C.P. Rinsland, A. Barbe, A. Hamdouni, J.-M. Flaud, and C. Camy-Peyret, Isotopic ozone in the 5μ region from high resolution balloon-borne and ground-based FTIR solar spectra, *J. Quant. Spectrosc. & Radiat. Transfer*, 59, 231-244, 1998.

Goldman, A., R.R. Gamache, A. Perrin, J.-M. Flaud, C.P. Rinsland, and L.S. Rothman, HITRAN Partition Functions and Weighted Transition Probabilities, *J. Quant. Spectrosc. & Radiat. Transfer*, to be submitted.

Heyart, M. A. Perrin, J.-M. Flaud, C. Camy-Peyret, C. P. Rinsland, M. A. H. Smith, and V., Malathy Devi, The v_1 and v_3 bands of $^{16}O^{17}O^{16}O$ line positions and intensities, *J. Molec. Spectrosc.*, *156*, 210-216, 1992.

Heyart, M., A. Perrin, J.-M. Flaud, C. Camy-Peyret, C.P. Rinsland, M.A.H. Smith, and V. Malathy Devi, The hybrid-type bands v_1 and v_3 of $^{16}O^{16}O^{17}O$ line positions and intensities, *J. Molec. Spectrosc.*, *157*, 524-531, 1993.

Malathy Devi, V. D. C. Benner, C.P. Rinsland, M.A.H. Smith, and D.S.Parmar, Infrared Spectroscopy of the CO_2 Molecule, Recent Res. Devel. in *Geophys Res.*, *1*, 119-148, 1996.

Malathy Devi, V., D. C. Benner, C.P. Rinsland, and M.A.H. Smith, Absolute Rovibrational Intensities of $^{12}C^{16}O_2$ Absorption Bands in the 3090 to 3800-cm^{11} Spectral Region. *J. Quant. Spectrosc. Radiat. Transfer*, 60, 741-770 1998a.

Malathy Devi, V., D. C. Benner, C.P. Rinsland, M.A.H. Smith, and D.S.Parmar, Infrared Spectroscopy of the CO_2 Molecule: *Research Signpost: Recent Research Developments in Geophysical Research*, Vol. 1, pp. 119-148, S. G. Pandalai, editor, 1997.

Malathy Devi, V., D. C. Benner, M.A.H. Smith, and C.P. Rinsland, Air and N_2 Broadening Coefficients and Pressure Shift Coefficients in the $^{12}C^{16}O_2$ Laser Bands, 52nd Ohio State University International Symposium on Molecular Spectroscopy, paper RF14, June 16-20, 1997.

Malathy Devi, V., D. C. Benner, M.A.H. Smith, and C.P. Rinsland, Self-Broadening and Self-Shift Coefficients in the Fundamental Band of CO. *J. Quant. Spectrosc. Radiat. Transfer*, *60,* 815-824, 1998b.

Malathy Devi, V., D. C. Benner, M.A.H. Smith, and C.P. Rinsland, Pressure-Broadening and Shift Coefficients in the 2 v_2^0 and v_1 Bands of $^{16}O^{13}C^{18}O$. 52nd Ohio State University International Symposium on Molecular Spectroscopy, paper RF13, June 16-20, 1997.

Malathy Devi, V., D. C. Benner, M.A.H. Smith, and C.P. Rinsland, Pressure-Broadening and Pressure Shift Coefficients in the $2v_2^0$ and v_1 Bands of $^{16}O^{13}C^{18}O$. *J. Quant. Spectrosc. Radiat. Transfer*, 60, 771-783, 1998.

Malathy Devi, V., D. C. Benner, M.A.H. Smith, and C.P. Rinsland, Air- and N_2 Broadening Coefficients and Pressure-shift Coefficients in the $^{12}C^{16}O_2$ Laser Bands. *J. Quant. Spectrosc. Radiat. Transfer*, *59*, 137-150, 1998.

Mandin, J.-Y., V. Dana, A. Perrin, J.-M. Flaud, C. Camy-Peyret, L. Régalia, and A. Barbe, The { $v_1 + 2 v_2, v_1 + v_3$} bands of NO_2: Line positions and intensities; Line intensities in the $v_1 + v_2 + v_3 - v_2$ hot band, *J. Mol. Spectrosc.*, *181*, 379-388, 1997.

Perrin, A., J.-M. Flaud, and C. Camy-Peyret , Calculated line positions and intensities for the $v_1 + v_3$ and $v_1 + v_2 + v_3 - v_2$ band of NO_2, *Infrared Phys.*, *22*, 343-348, 1982.

Perrin, A., J.-M. Flaud, F. Keller, A. Goldman, R.D. Blatherwick, F.J. Murcray, and C.P. Rinsland, New analysis of the $\nu_8 + \nu_9$ band of HNO_3: Line positions and intensities, *J. Molec. Spectrsoc.*, submitted, 1998.

Pine, A. S., and C. P. Rinsland, The role of torsional hot bands in modeling atmospheric ethane, *53rd International Molecular Spectroscopy Symposium,* Columbus, OH, paper TF17, 1998.

Rinsland, C. P.; J.-M. Flaud, A. Goldman, A. Perrin, C. Camy-Peyret, M.A.H Smith, V. Malathy Devi, D.C. Benner, A. Barbe, T.M. Stephen, and F.J.Murcray,: Spectroscopic Parameters for Ozone and Its Isotopes: Current Status, Prospects for Improvement, and the Identification of $^{16}O^{16}O^{17}O$ and $^{16}O^{17}O^{16}O$ Lines in Infrared Ground-Based and Stratospheric Solar Absorption Spectra. *J. Quant. Spectrosc. Radiat. Transfer*, *60,* 803-814, 1998.

Rinsland, C. P.; M.R. Gunson, P. Wang, R.F. Arduini, B.A. Baum, P. Minnis, A. Goldman, M.C. Abrams, R. Zander, E. Mahieu, R.J. Salawitch, H.A. Michelsen, F.W. Irion, and M.J.Newchurch, ATMOS/ATLAS 3 Infrared Profile Measurements of Clouds in the Tropical and Subtropical Upper Troposphere. *J. Quant. Spectrosc. Radiat. Transfer*, *60,* 903-919, 1998.

Rinsland, C. P., N.B.Jones, B. Connor, J.A. Logan, N.S. Pougatchev, A. Goldman, F.J. Murcray,T.M. Stephen, A.S. Pine, R. Zander, E. Mahieu, and E. Demoulin, Northern and Southern Hemisphere Ground-Based Infrared Spectroscopic Measurements of Tropospheric Carbon Monoxide and Ethane, *J. Geophys. Res.*, 60, 665-710, 1998.

Rinsland, C. P.; A. Goldman, and J.-M.Flaud, Infrared Spectroscopic Parameters of COF_2, SF_6, ClO, N_2, and O_2, *J. Quant. Spectrosc. Radiat. Transfer*, *48*, 693-699, 1992.

Rothman, L.S., C.P. Rinsland, A. Goldman, S.T. Massie, D.P. Edwards, J.-M. Flaud, A. Perrin, C. Camy-Peyret, V. Dana, J.-Y. Mandin, J. Schroeder, A. McCann, R.R. Gamache, R.B. Wattson, K. Yoshino, K.V. Chance, K.W. Jucks, L.R. Brown, V. Nemtchinov, and P. Varanasi, The HITRAN Molecular Spectroscopic Database and HAWKS (HITRAN Atmospheric Workstation): 1996 Edition, *J. Quant. Spectrosc. Radiat. Transfer*, *60,* 665-710, 1998.

Sen, B.; G.C. Toon, G.B. Osterman, J.-F. Blavier, J.J. Margitan, R.J. Salawitch, and G.K.Yue, Measurements of reactive nitrogen in the stratosphere, *J. Geophys. Res., 103*, 3571-3585, 1998.

Smith, M. A. H., C. P. Rinsland, V. Malathy Devi, and D. C. Benner, Absolute intensities of O_3 lines in the 9-11 μm region, *53rd Ohio State University International Symposium on Molecular Spectroscopy, paper WF04,* Columbus, OH, 1998.

Toth, R. A., $HD^{16}O$, $HD^{18}O$, and $HD^{17}O$ Transition Frequency and Strengths in the ν_2 Bands, *J. Mol. Spectrosc.*, *162*, 20-40, 1993.

Wang, W. F., P.P.Ong, T.L. Tan, E.C. Looi, and H.H. Teo, Infrared analysis of the anharmonic resonance between $\nu_8 + \nu_9$ and the dark state $\nu_6 + \nu_7$, *J. Mol. Spectrosc.*, *183*, 407-412, 1997.

LAST PAGE